High performance supercapacitors based on wood-derived thick carbon electrodes synthesized via green activation process

Bing Yan[a], Li Feng[a], Jiaojiao Zheng[a], Qian Zhang[b, *], Shaohua Jiang[a], Chunmei Zhang[c], Yichun Ding[d, *], Jingquan Han[a], Wei Chen[e, f, *], Shuijian He[a, *]

[a] *International Innovation Center for Forest Chemicals and Materials, Co-Innovation Center of Efficient Processing and Utilization of Forest Resources, College of Materials Science and Engineering, Nanjing Forestry University, Nanjing, 210037, China.*

[b] *College of Science, Nanjing Forestry University, Nanjing 210037, China.*

[c] *Institute of Materials Science and Devices, School of Materials Science and Engineering, Suzhou University of Science and Technology, Suzhou 215009, China.*

[d] *Fujian Institute of Research on the Structure of Matter, Chinese Academy of Sciences, Fuzhou 350010, China.*

[e] *State Key Laboratory of Electroanalytical Chemistry, Changchun Institute of Applied Chemistry, Chinese Academy of Sciences, Changchun 130022, Jilin, PR China.*

[f] *University of Science and Technology of China, Hefei 230026, PR China.*

* Corresponding authors

E-mail: zhangqian5689@njfu.edu.cn (Qian Zhang); ycding@fjirsm.ac.cn (Yichun Ding); weichen@ciac.ac.cn (Wei Chen); shuijianhe@njfu.edu.cn (Shuijian He)

Details about electrochemical calculations

CV is an effective analysis means for exploring the electrochemical kinetics of electrodes. According to the Duun's method [1], the relationship between peak current (i) with disparate scanning rates (v) can be described in the following equations:

$$i = a \times v^b \qquad (1)$$

$$logi = b \times logv + loga \qquad (2)$$

The b value depended on the slope of the $log\ i$ with respect to $log\ v$, the b value of 0.5 is indicative of a diffusion-controlled process, while $b = 1$ represents a fast capacitive process.

By separating the total current response (i) at a given voltage, the contribution can be quantitatively separated into capacitive-controlled process and diffusion-controlled process according to the following equation:

$$i = k_1 v + k_2 v^{1/2} \qquad (3)$$

Where the $k_1 v$ and $k_2 v^{1/2}$ correspond to capacitive- and diffusion-controlled contribution, respectively.

In three-electrode system, the areal specific capacitances (C_s, mF cm^{-2}) and gravimetric specific capacitances (C_g, F g^{-1}) of a single electrode was calculated from GCD curves according to equations (4) and (5), respectively. The volumetric specific capacitances (C_V, F cm^{-3}) of single electrode was calculated from C_s by the formula (6).

$$Cs = \frac{I\Delta t}{s\Delta V} \qquad (4)$$

$$Cg = \frac{I\Delta t}{m\Delta V} \qquad (5)$$

$$CV = \frac{Cs}{d} \qquad (6)$$

Where I (A), Δt (s), s (cm^2), d (cm), m (g), ΔV (V) represents the discharge current, galvanostatic discharge time, the geometry area, thickness and mass of working electrode, the potential window of the discharge process, respectively.

In two-electrode system, the C'_s (mF cm^{-2}), C'_g (F g^{-1}) and C'_V (F cm^{-3}) were calculated from GCD curves by the equations (7) to (9).

$$C's = \frac{2 \times I \times \Delta t}{s \times \Delta V} \qquad (7)$$

$$C'g = \frac{2 \times I \times \Delta t}{m \times \Delta V} \qquad (8)$$

$$C'V = \frac{C's}{d} \qquad (9)$$

The areal energy density (E_s, mWh cm^{-2}), areal power density (P_s, mW cm^{-2}), gravimetric energy density (E_g, Wh kg^{-1}), gravimetric power density (P_g, W kg^{-1}), volumetric energy density (mWh cm^{-3}) and volumetric power density (mW cm^{-3}) was based on the calculated capacitance values and evaluated according to the following equation:

$$Es = \frac{C'_s \times \Delta V^2}{7200} \qquad (10)$$

$$Ps = \frac{3600 \times E_S}{\Delta t} \qquad (11)$$

$$Eg = \frac{C'_g \times \Delta V^2}{7.2} \qquad (12)$$

$$Pg = \frac{3600 \times E_g}{\Delta t} \qquad (13)$$

$$EV = \frac{Es}{d} \qquad (14)$$

$$PV = \frac{Ps}{d} \qquad (15)$$

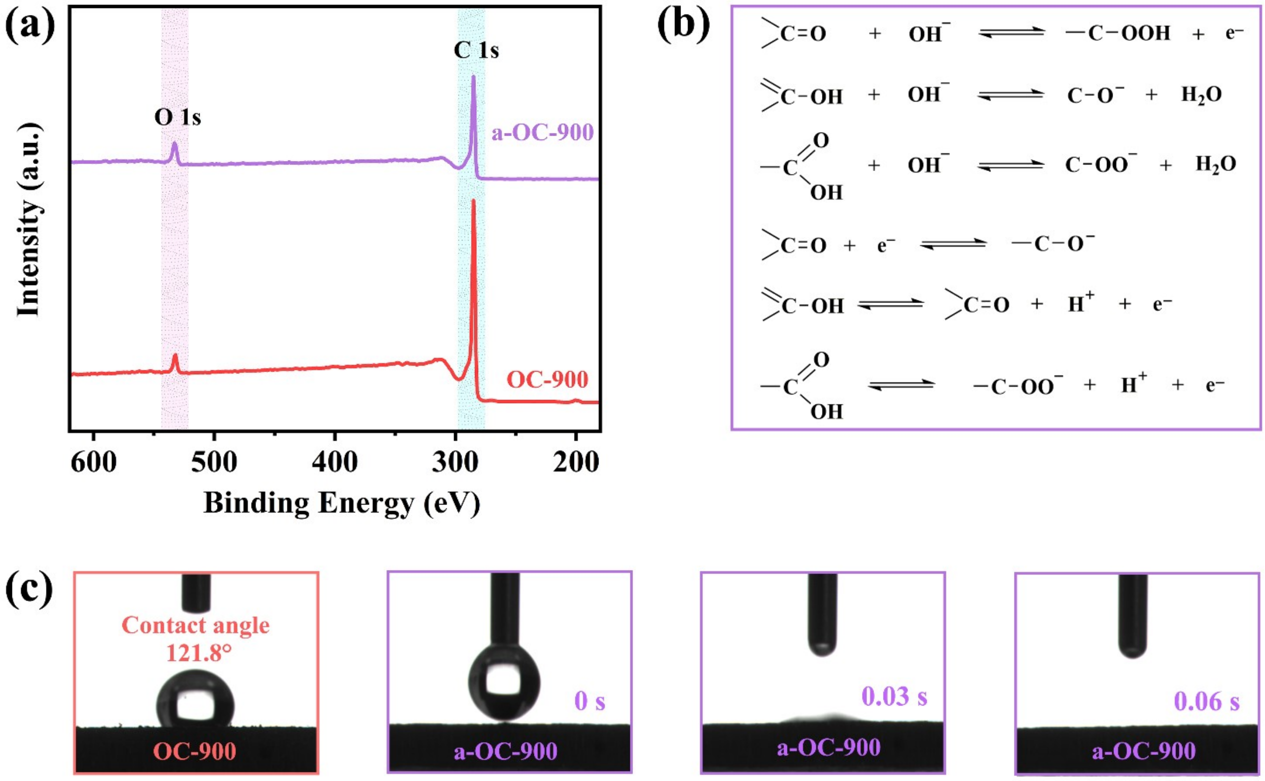

Fig. S1. (a) XPS survey spectra of OC-900 and a-OC-900. (b) Faradaic redox reactions involved in the alkaline/ acidic electrolyte. (c) Water contact angle measurement of OC-900 (red) and a-OC-900 (purple).

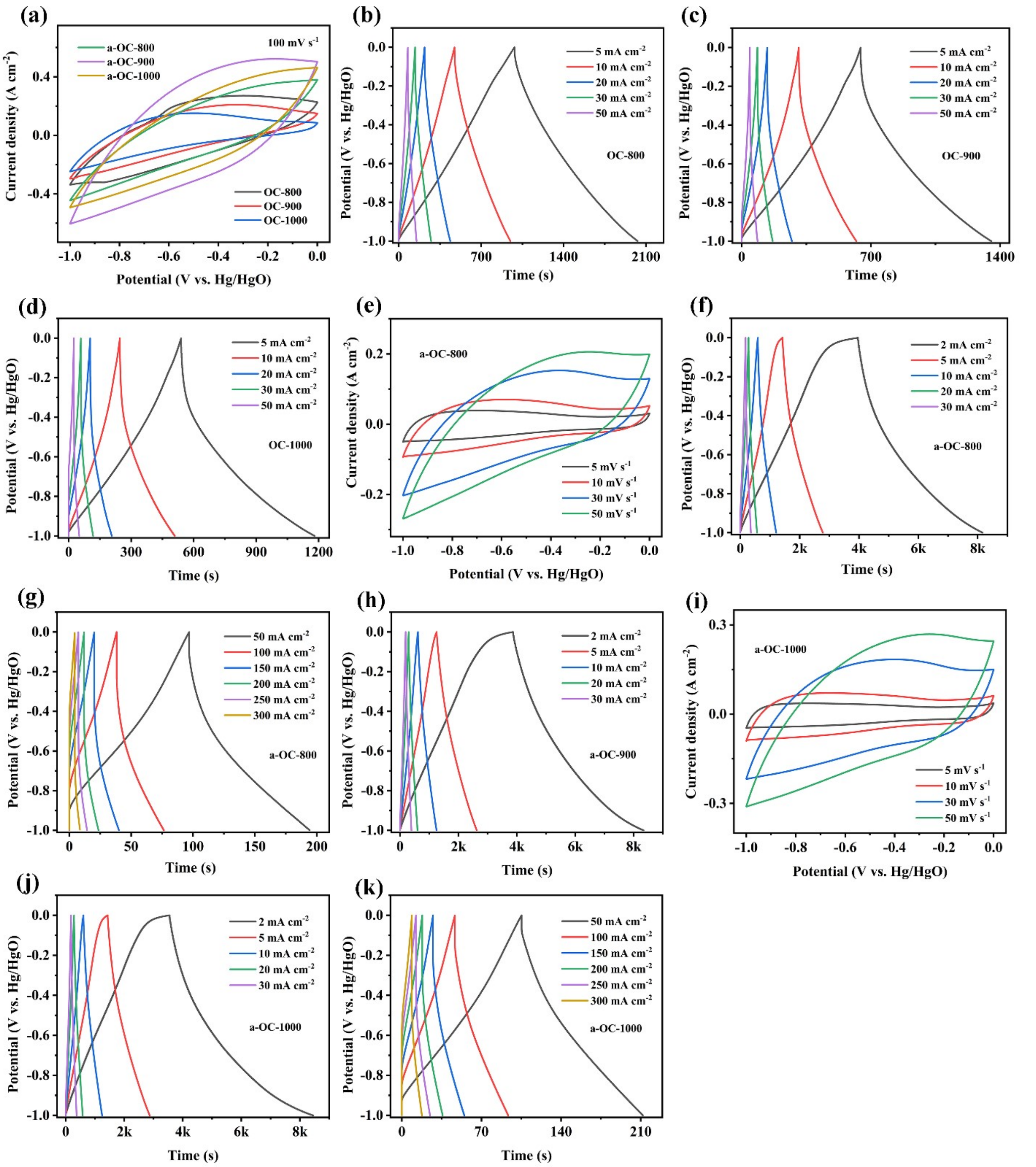

Fig. S2. Capacitive properties of electrodes in three-electrode system with 6 M KOH electrolyte. (a) The comparison of CV curves of OC-X and activated samples at 100 mV s^{-1}. The GCD profiles of (b) OC-800, (c) OC-900 and (d) OC-1000, respectively. (e) CV curves and (f, g) GCD profiles of a-OC-800. (h) GCD profiles of a-OC-900. (i) CV curves and (j, k) GCD profiles of a-OC-1000.

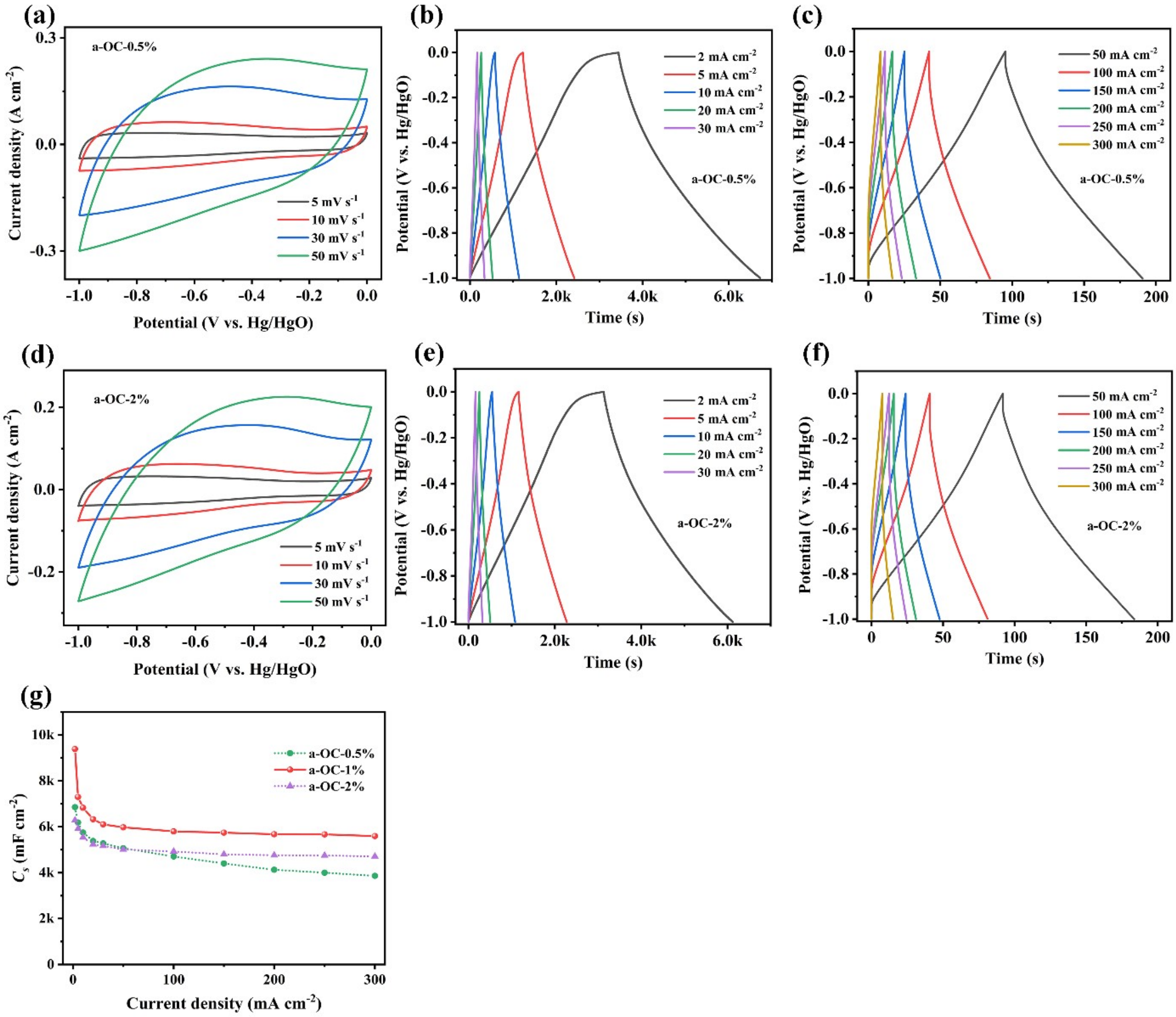

Fig. S3. Capacitive properties of concentration series samples in three-electrode system with 6 M KOH electrolyte. (a) CV curves and (b, c) GCD profiles of a-OC-0.5%. (d) CV curves and (e, f) GCD profiles of a-OC-2%. (g) Rate performance of concentration series samples.

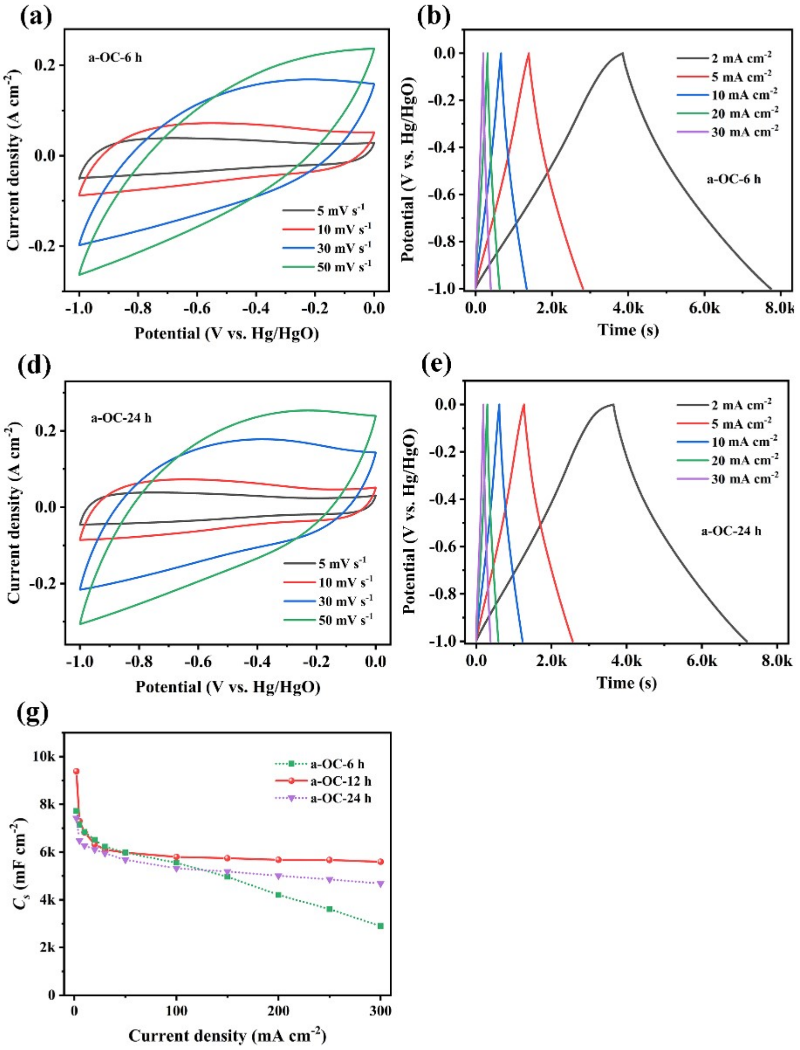

Fig. S4. Capacitive properties of activation time series samples in three-electrode system with 6 M KOH electrolyte. (a) CV curves and (b, c) GCD profiles of a-OC-6 h. (d) CV curves and (e, f) GCD profiles of a-OC-24 h. (g) Rate performance of activation time series samples.

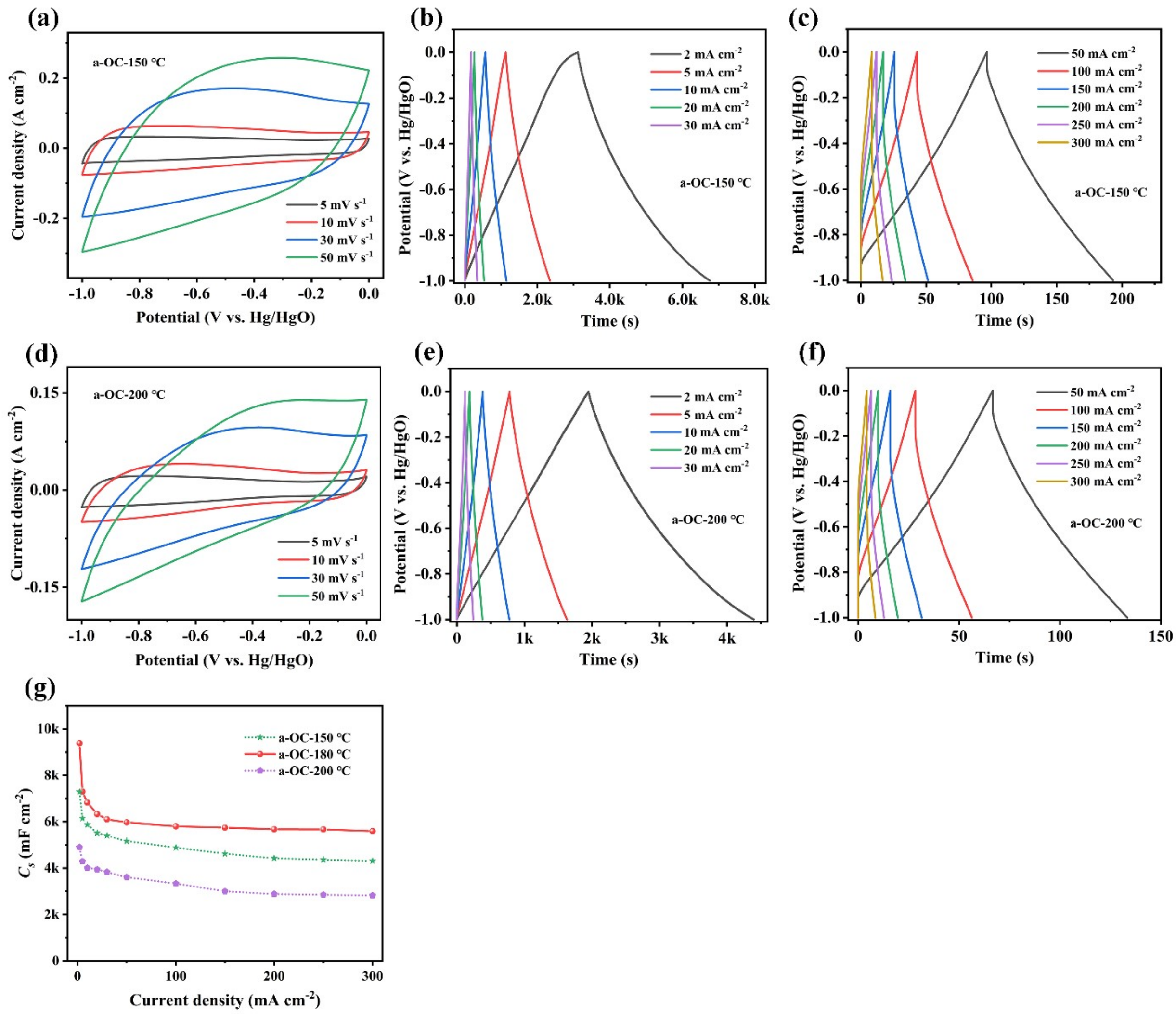

Fig. S5. Capacitive properties of activation temperature series samples in three-electrode system with 6 M KOH electrolyte. (a) CV curves and (b, c) GCD profiles of a-OC-150 °C. (d) CV curves and (e, f) GCD profiles of a-OC-200 °C. (g) Rate performance of activation temperature series samples.

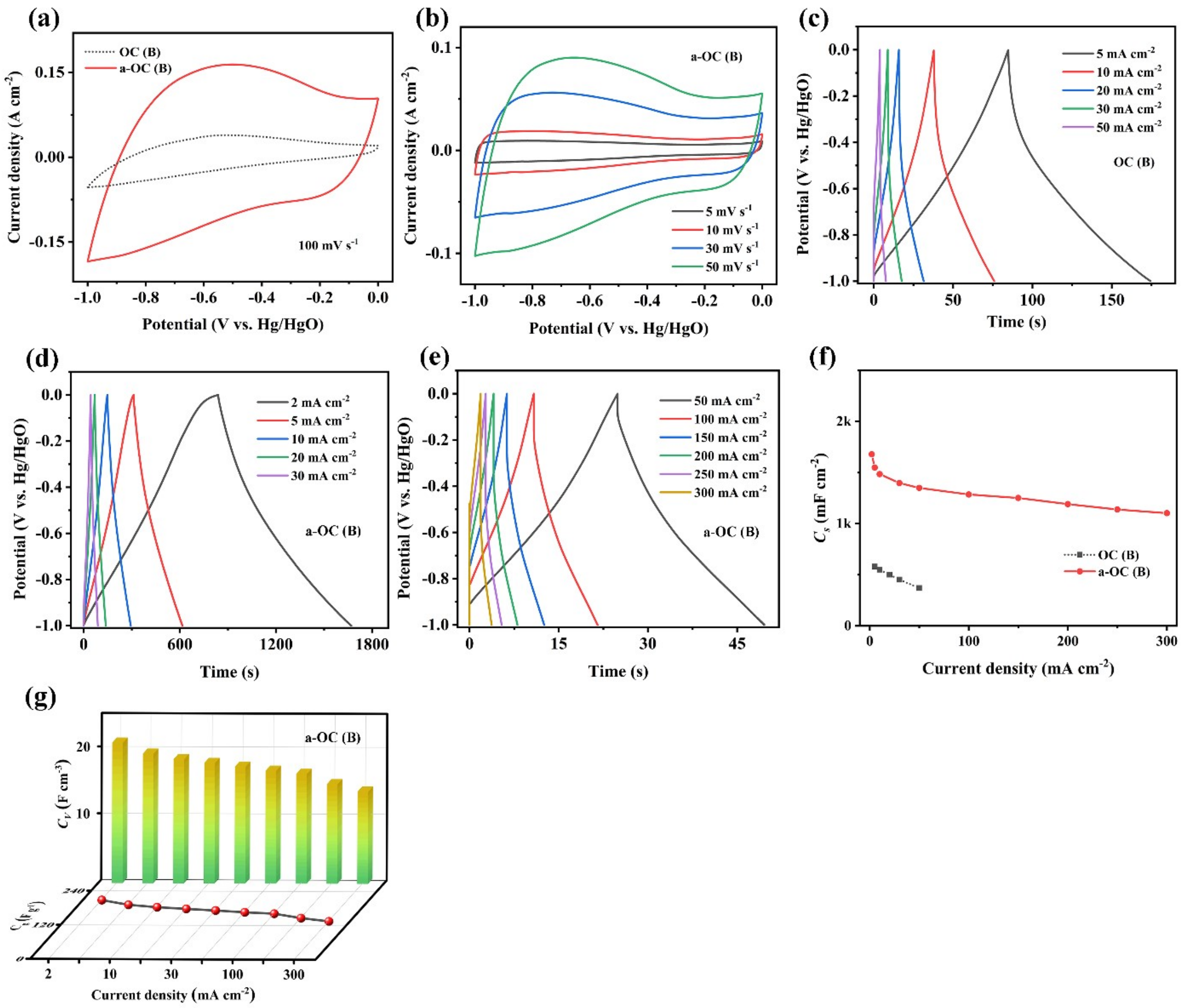

Fig. S6. Capacitive properties of electrodes in three-electrode system with 6 M KOH electrolyte. (a) The comparison of CV curves of OC (B) and a-OC (B) at 100 mV s^{-1}. (b) CV curves of a-OC (B). GCD profiles of (c) OC (B) and (d, e) a-OC (B). (f) Rate performance of OC (B) and a-OC (B). (g) Comparison of C_g and C_V versus different current densities of a-OC (B).

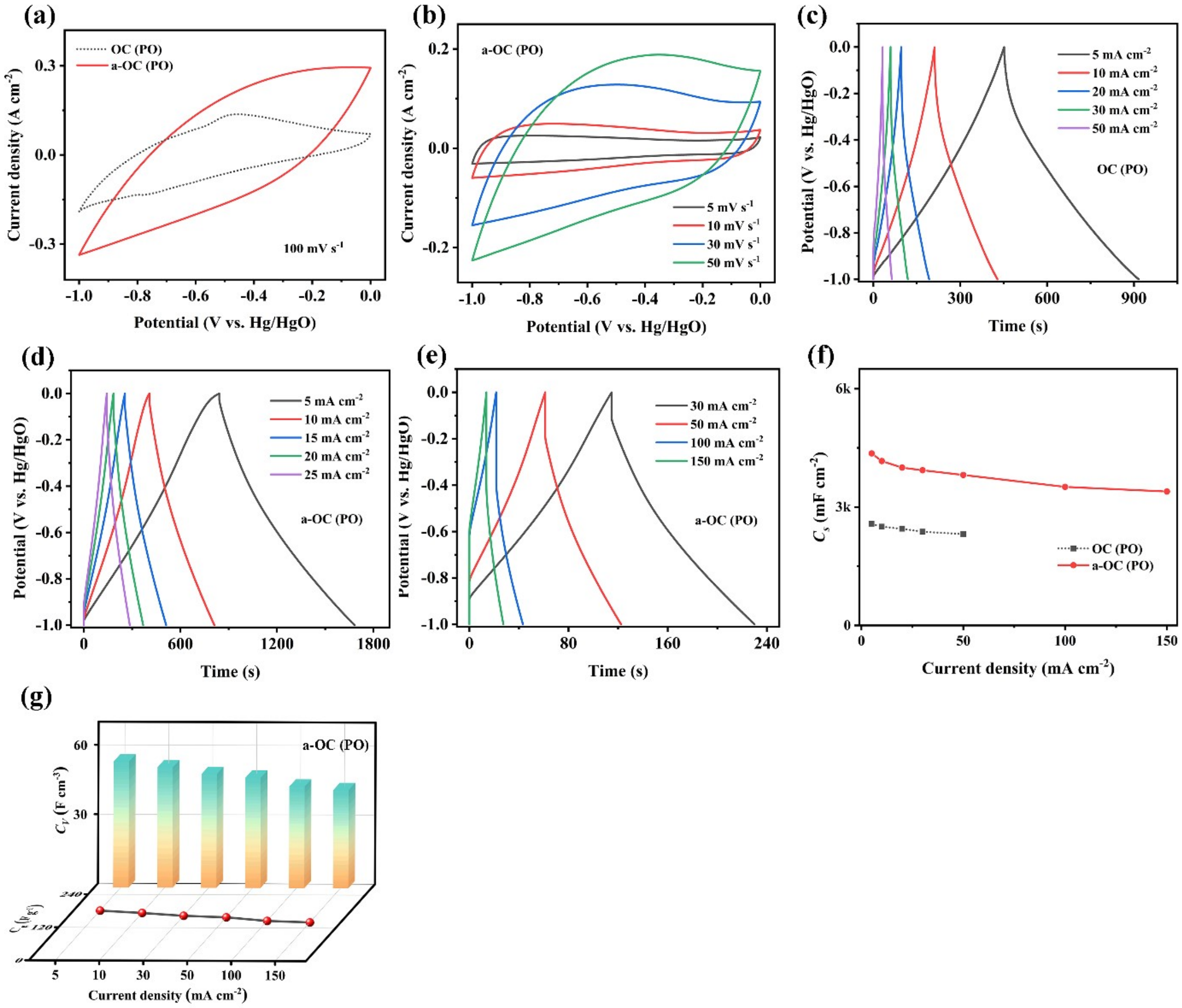

Fig. S7. Capacitive properties of electrodes in three-electrode system with 6 M KOH electrolyte. (a) The comparison of CV curves of OC (PO) and a-OC (PO) at 100 mV s^{-1}. (b) CV curves of a-OC (PO). GCD profiles of (c) OC (PO) and (d, e) a-OC (PO). (f) Rate performance of OC (PO) and a-OC (PO). (g) Comparison of C_g and C_V versus different current densities of a-OC (PO).

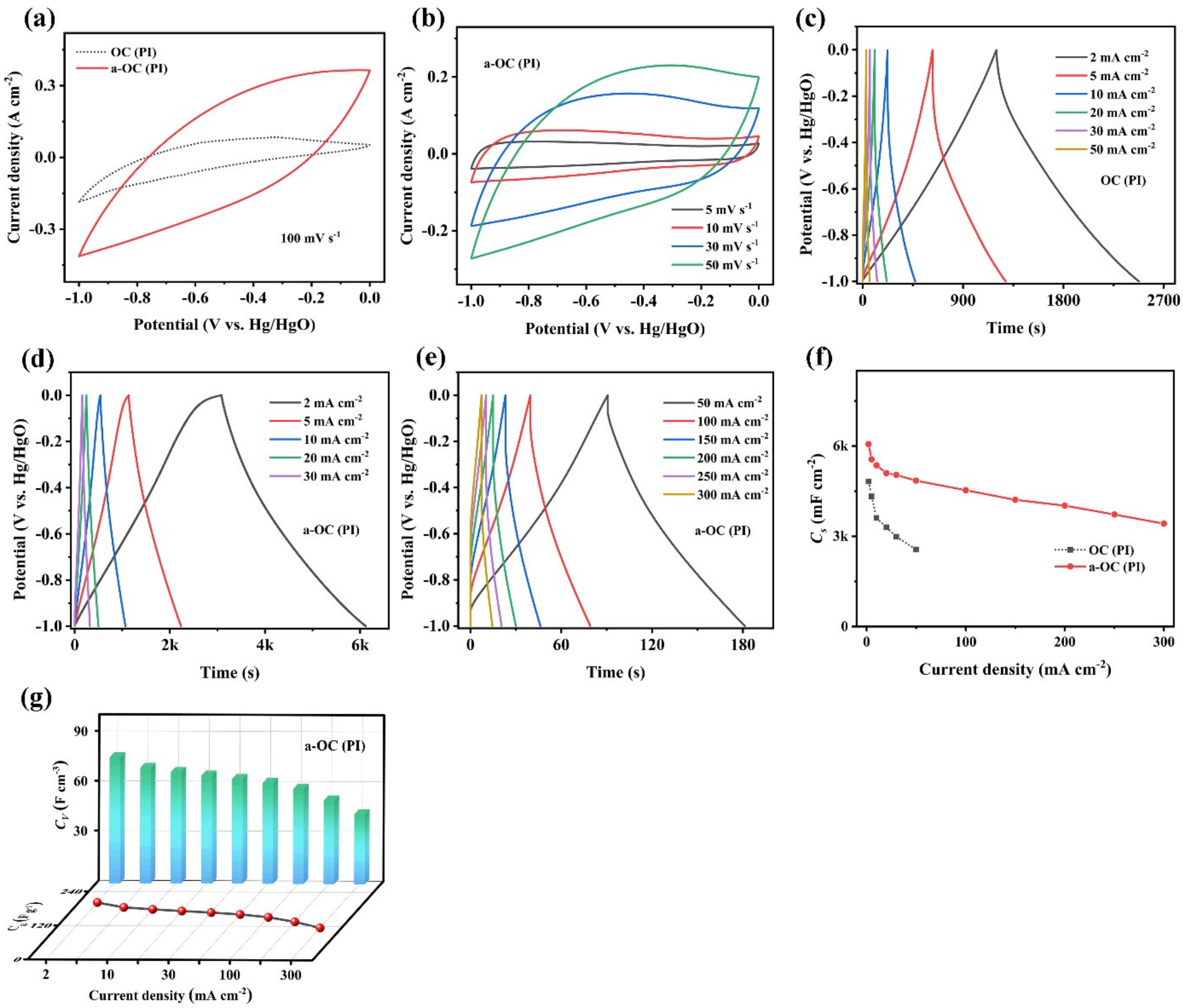

Fig. S8. Capacitive properties of electrodes in three-electrode system with 6 M KOH electrolyte. (a) The comparison of CV curves of OC (PI) and a-OC (PI) at 100 mV s^{-1}. (b) CV curves of a-OC (PI). GCD profiles of (c) OC (PI) and (d, e) a-OC (PI). (f) Rate performance of OC (PI) and a-OC (PI). (g) Comparison of C_g and C_V versus different current densities of a-OC (PI).

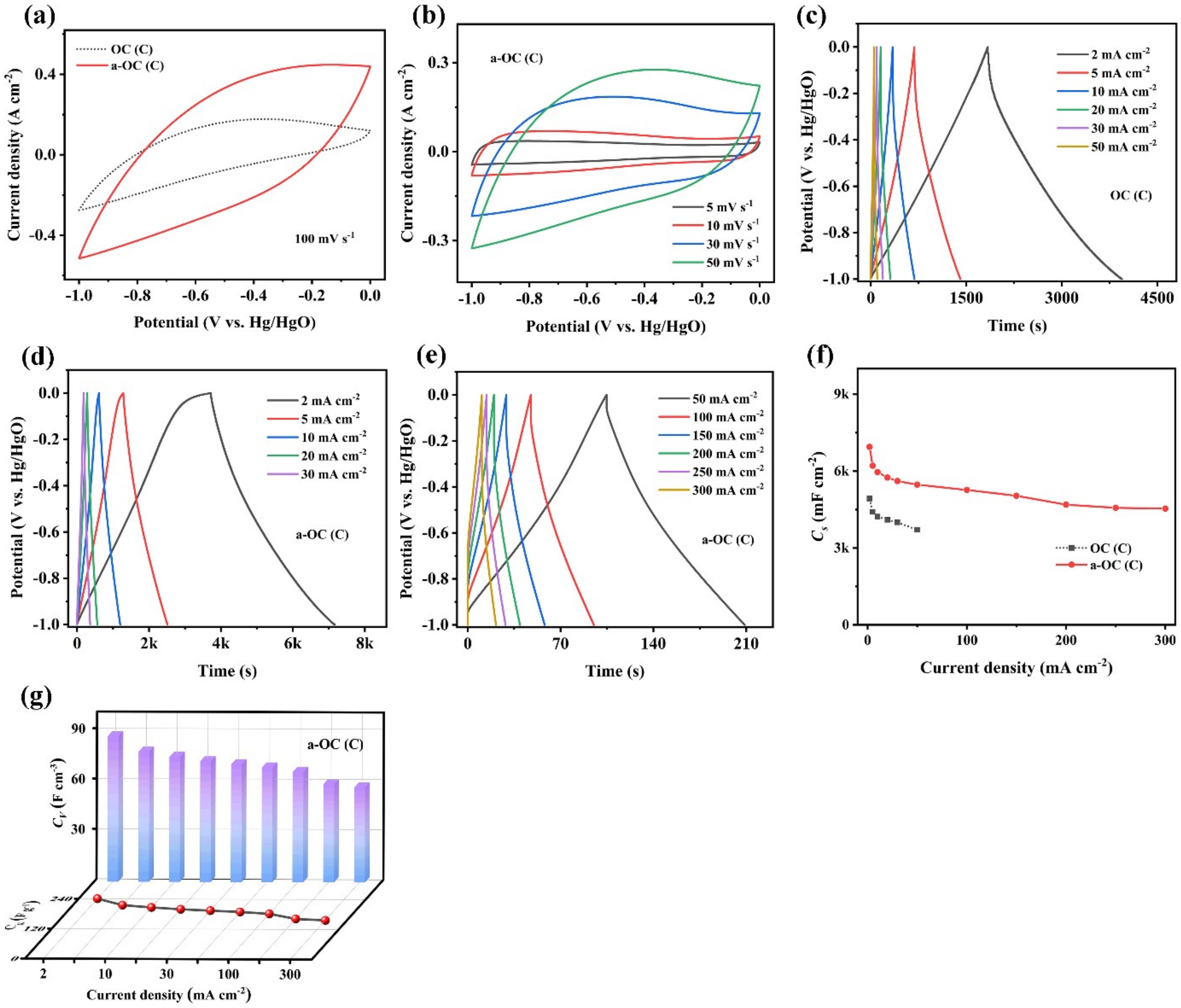

Fig. S9. Capacitive properties of electrodes in three-electrode system with 6 M KOH electrolyte. (a) The comparison of CV curves of OC (C) and a-OC (C) at 100 mV s^{-1}. (b) CV curves of a-OC (C). GCD profiles of (c) OC (C) and (d, e) a-OC (C). (f) Rate performance of OC (C) and a-OC (C). (g) Comparison of C_g and C_V versus different current densities of a-OC (C).

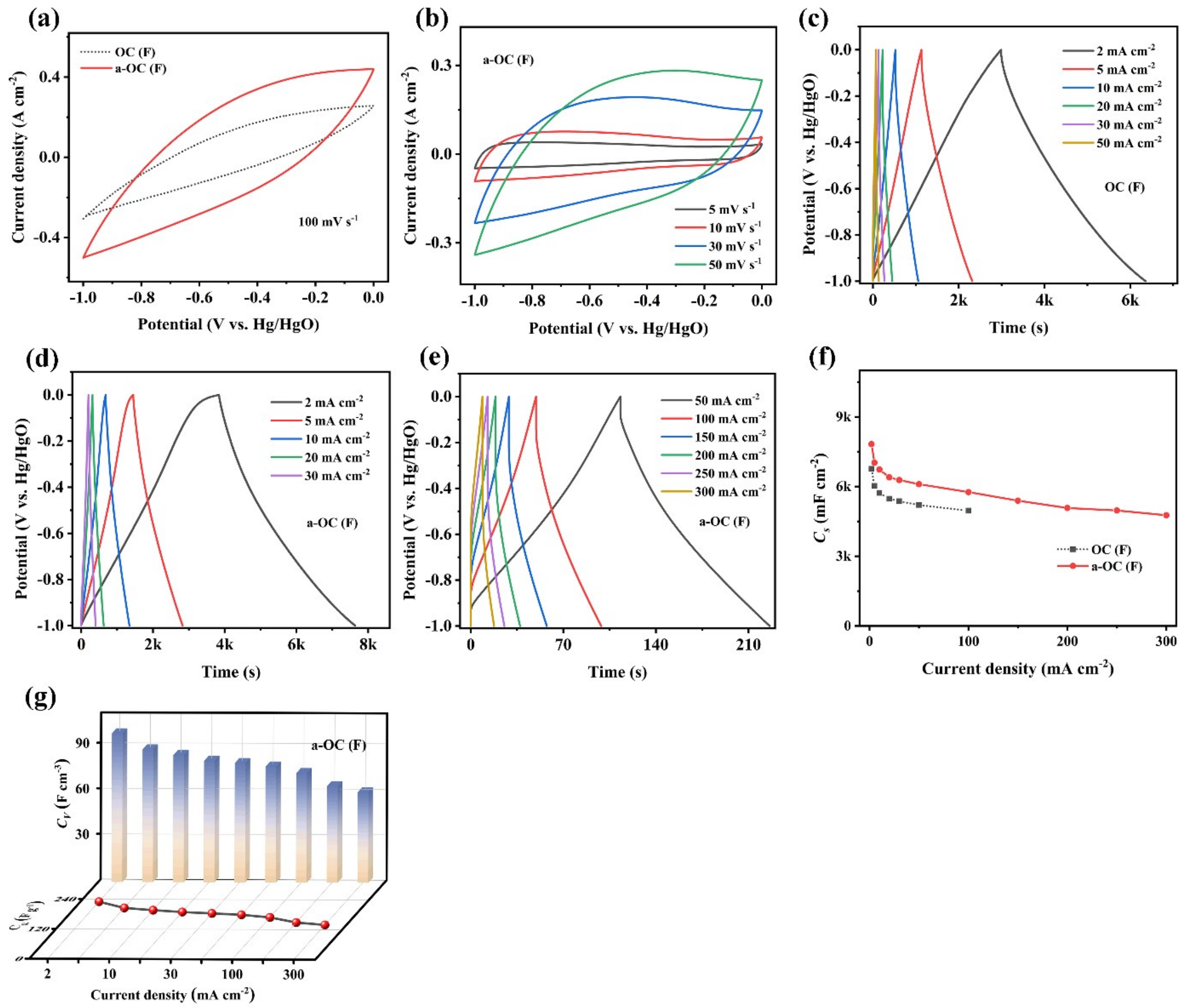

Fig. S10. Capacitive properties of electrodes in three-electrode system with 6 M KOH electrolyte. (a) The comparison of CV curves of OC (F) and a-OC (F) at 100 mV s^{-1}. (b) CV curves of a-OC (F). GCD profiles of (c) OC (F) and (d, e) a-OC (F). (f) Rate performance of OC (F) and a-OC (F). (g) Comparison of C_g and C_V versus different current densities of a-OC (F).

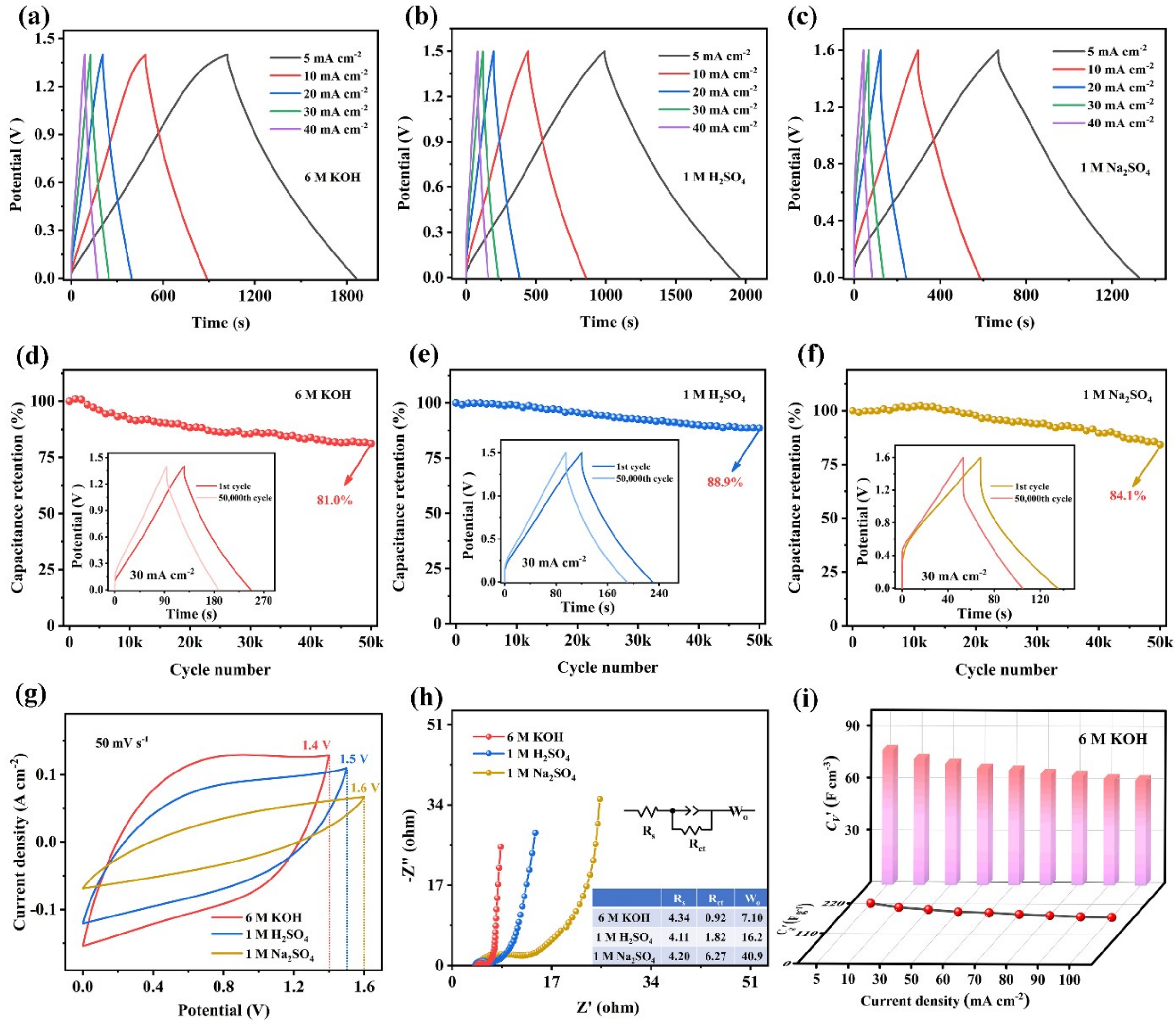

Fig. S11. The capacitive properties of symmetric supercapacitors (a-OC-900//a-OC-900) with 6 M KOH, 1 M H_2SO_4, and 1 M Na_2SO_4 electrolyte, respectively. The GCD profiles of devices in (a) 6 M KOH, (b) 1 M H_2SO_4, and (c) 1 M Na_2SO_4 electrolyte. The long cycle performance of devices in (d) 6 M KOH, (e) 1 M H_2SO_4, and (f) 1 M Na_2SO_4 electrolyte. (g) The comparison of CV curves of devices in different electrolytes. (h) Nyquist plots of devices in different electrolytes, the inset is the corresponding equivalent circuit diagram and fitted values. (i) Comparison of C_g and C_V versus different current densities of devices in 6 M KOH.

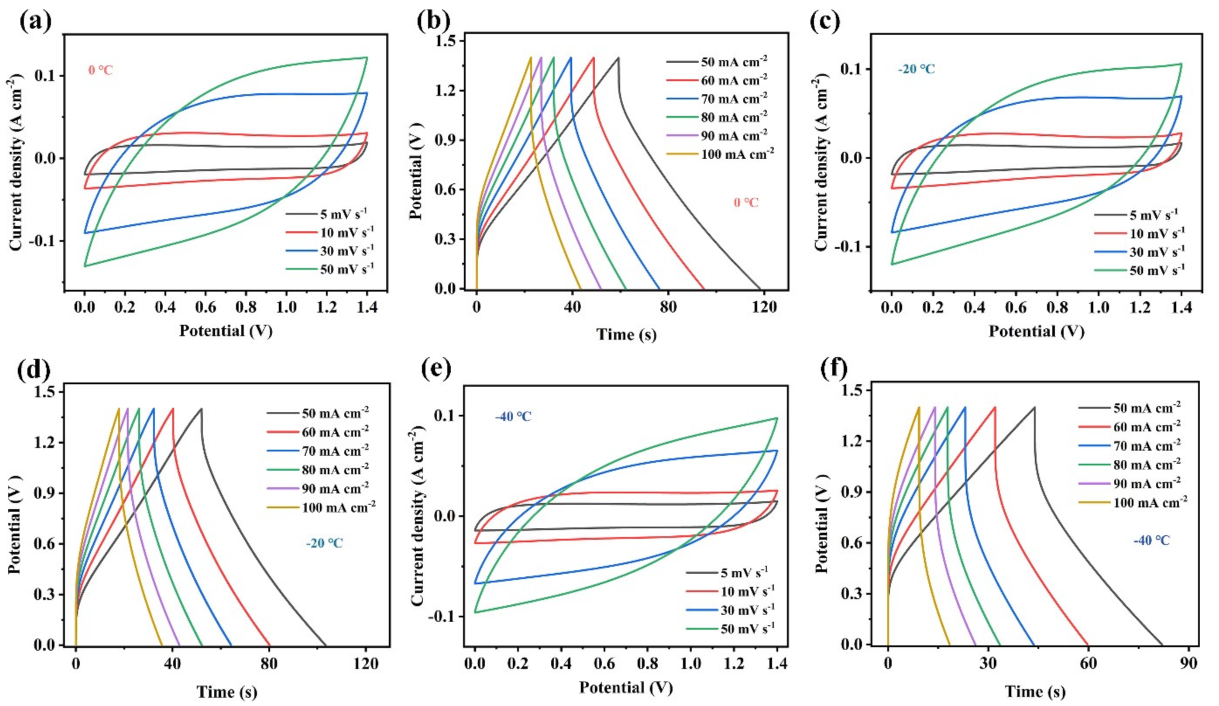

Fig. S12. The capacitive properties of symmetric supercapacitors (a-OC-900//a-OC-900) with 6 M KOH at different temperature. (a) CV curves and (b) GCD profiles of devices at 0 ℃. (c) CV curves and (d) GCD profiles of devices at -20 ℃. (e) CV curves and (f) GCD profiles of devices at -40 ℃.

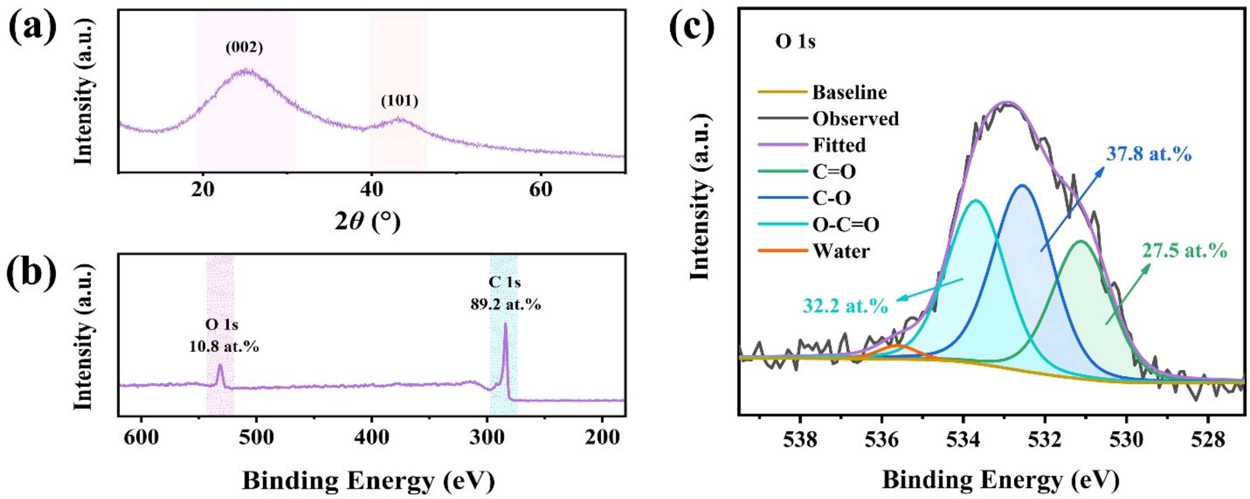

Fig. S13. (a) XRD pattern, (b) XPS survey spectrum, and (c) high-resolution O 1s spectra of the a-OC-900 electrode after 70,000 cycles at -40 °C.

Table S1. Porosity characteristics of OC-800, OC-900, OC-1000, a-OC-800, a-OC-900, a-OC-1000.

Sample	S_{BET} ($m^2\ g^{-1}$)	S_{mic} ($m^2\ g^{-1}$)	V_t ($cm^3\ g^{-1}$)	V_{mic} ($cm^3\ g^{-1}$)	V_{mic}/V_t (%)	D_{ap} (nm)
OC-800	371.6	348.2	0.20	0.18	90	2.19
OC-900	300.2	282.3	0.17	0.15	88	1.59
OC-1000	204.8	200.5	0.13	0.12	92	1.09
a-OC-800	722.8	601.8	0.35	0.26	74	1.95
a-OC-900	612.6	552.4	0.30	0.21	70	1.89
a-OC-1000	532.4	487.2	0.25	0.22	88	1.86

S_{BET}, total specific surface area.

S_{mic}, specific surface area of micropores.

V_t, total pore volume.

V_{mic}, micropore volume.

D_{ap}, average pore diameter.

Table S2. Element analysis of OC-900 and a-OC-900

Samples	C (at.%)	O (at.%)	O/C	C 1s					O 1s			
				C=C (BE, at.%)	C-O (BE, at.%)	C=O (BE, at.%)	O-C=O (BE, at.%)	π-π* (BE, at.%)	O-I (BE, at.%)	O-II (BE, at.%)	O-III (BE, at.%)	Chemisorbed/ physisorbed water
OC-900	95.5	4.5	0.05	284.8, 56.1	285.4, 22.8	286.6, 10.5	288.8, 8.3	291.0, 2.4	530.6, 11.8	532.5, 67.9	534.3, 14.8	536.7, 6.1
a-OC-900	89.5	10.5	0.12	284.8, 62.0	285.8, 10.7	286.9, 15.9	289.0, 6.0	291.0, 5.4	531.1, 32.7	532.7, 29.2	533.9, 32.1	535.9, 6.0

BE: Binding energy, eV.

at.%: atomic content ratios.

Table S3. The comparison of a-OC-900 and other carbon-based electrodes with high mass loading (three-electrode system).

Precursor	Method	Electrode mass loading; thickness	Electrolyte	Initial capacitance	Rate performance	Cycle durability	Ref.
Basswood	H_2O_2 activation	~40 mg cm^{-2} ~800 μm	6 M KOH	9383.7 mF cm^{-2}, 330.2 F g^{-1}, 117.5 F cm^{-3} at 2 mA cm^{-2}	5592.0 mF cm^{-2}, 200.1 F g^{-1}, 69.9 F cm^{-3} at 300 mA cm^{-2}	96.8% 50,000 100 mA cm^{-2}	This work
Peanut dregs	KOH activation	12.5 mg cm^{-2} 125 μm	6 M KOH	4102 mF cm^{-2}, 328 F g^{-1}, 328 F cm^{-3} at 10 mA cm^{-2}	3484 mF cm^{-2}, at 200 mA cm^{-2}	94% 20,000 20 mA g^{-1}	[2]
Basswood	Phytic acid activation	17.17 mg cm^{-2} ~800 μm	6 M KOH	6590 mF cm^{-2}, 384 F g^{-1}, at 1 mA cm^{-2}	4990 mF cm^{-2}, 285 F g^{-1}, at 30 mA cm^{-2}	90.5% 20,000 20 mA cm^{-2}	[3]
Basswood	Enzymolysis-treated	~25 mg cm^{-2} ~800 μm	6 M KOH	8410 mF cm^{-2}, 328 F g^{-1}, at 1 mA cm^{-2}	3776 mF cm^{-2}, 146.9 F g^{-1}, at 50 mA cm^{-2}	87% 15,000 50 mA cm^{-2}	[4]
Basswood	CO_2 activation	30 mg cm^{-2} 1 mm	1 M Na_2SO_4	3204 mF cm^{-2}, 118.7 F g^{-1}, at 1 mA cm^{-2}	2800 mF cm^{-2}, 103.7 F g^{-1}, at 30 mA cm^{-2}	/	[5]
Resin 3D printing	CO_2 activation	46.2 mg cm^{-2} 1.5 mm	1 M Na_2SO_4	5251 mF cm^{-2}, 115 F g^{-1}, at 3 mA cm^{-2}	4273 mF cm^{-2}, 93.5 F g^{-1}, at 30 mA cm^{-2}	91% 10,000 30 mA cm^{-2}	[6]
Basswood	Delignification	54.75 mg cm^{-2} 1.5 mm	6 M KOH	7600 mF cm^{-2}, 130 F g^{-1}, at 1 mA cm^{-2}	~5000 mF cm^{-2}, ~80 F g^{-1}, at 50 mA cm^{-2}	/	[7]

Table S4. The comparison of a-OC-900//a-OC-900 and other carbon-based devices with high mass loading (two-electrode system).

Precursor	Method	Electrode mass loading; thickness	Electrolyte	Initial capacitance	Rate performance	Cycle durability	Maximum energy density	Maximum power density	Ref.
Basswood	H_2O_2 activation	~40 mg cm^{-2} ~800 μm	6 M KOH	6205.7 mF cm^{-2}, 221.6 F g^{-1}, 77.6 F cm^{-3} at 5 mA cm^{-2}	4849.5 mF cm^{-2}, 173.2 F g^{-1}, 60.6 F cm^{-3} at 100 mA cm^{-2}	81% 50,000 30 mA cm^{-2}	1.64 mWh cm^{-2}, 58.8 Wh kg^{-1}, 20.6 mWh cm^{-3}	110.2 mW cm^{-2}, 3915.7 W kg^{-1} 1370.3 mW cm^{-3}	This work
Conductive carbon black	KOH, $MgSO_4$ activation	10 mg cm^{-2} 700 μm	6 M KOH	1280 mF cm^{-2}, 111 F g^{-1} 16.1 F cm^{-3} at 1 A g^{-1}	~950 mF cm^{-2}, 95 F g^{-1} at 10 A g^{-1}	92.6% 10,000 2 A g^{-1}	/	/	8
Waste cotton	KOH activation	10 mg cm^{-2} ~150 μm	6 M KOH	175 F g^{-1}, 129 F cm^{-3}, at 0.5 A g^{-1}	125 F g^{-1}, 100 F cm^{-3}, at 10 A g^{-1}	~90% 10,000 0.5 A g^{-1}	6.2 Wh kg^{-1}, 4.97 mWh cm^{-3}	/	9
PAN PMMA GO	layer-by-layer electrospinning	12 mg cm^{-2} 82 μm	1 M H_2SO_4	1536 mF cm^{-2}, 103 F cm^{-3} at 1 mA cm^{-2}	1030 mF cm^{-2}, 69 F cm^{-3} at 4 mA cm^{-2}	~99.4% 20,000 10 mA cm^{-2}	0.22 mWh cm^{-2}, 14.3 mWh cm^{-3}	10.3 mW cm^{-2}	10
Graphene	Phytic acid activation	12 mg cm^{-2} ~100 μm	6 M KOH	1148.5 mF cm^{-2}, 57.4 F cm^{-3} at 1 mA cm^{-2}	811 mF cm^{-2}, 40.5 F cm^{-3} at 100 mA cm^{-2}	89% 5,000 20 mA cm^{-2}	7.9 mWh cm^{-3}	2500 mW cm^{-3}	11

Precursor	Method	Electrode mass loading; thickness	Electrolyte	Initial capacitance	Rate performance	Cycle durability	Maximum energy density	Maximum power density	Ref.
Basswood	Phytic acid activation	17.17 mg cm^{-2} ~800 μm	6 M KOH	4700 mF cm^{-2}, 206.5 F g^{-1}, 29.3 F cm^{-3} at 1 mA cm^{-2}	2900 mF cm^{-2} 106 F g^{-1}, 18.1 F cm^{-3} at 20 mA cm^{-2}	90.5% 20,000 20 mA cm^{-2}	0.94 mWh cm^{-2}, 41.2 Wh kg^{-1},	14.4 mW cm^{-2}, 437.4 W kg^{-1}	[3]
Basswood	Enzymolysis-treated	~25 mg cm^{-2} ~800 μm	6 M KOH	1500 mF cm^{-2}, 79 F g^{-1} at 1 mA cm^{-2}	570 mF cm^{-2}, 30 F g^{-1} at 50 mA cm^{-2}	86.6% 15,000 20 mA cm^{-2}	0.21 mWh cm^{-2}, 10.97 Wh kg^{-1}	15.0 mW cm^{-2} 800 W kg^{-1}	[4]
rGO	H_2SO_4 treatment	33 mg cm^{-2} 260 μm	1 M H_2SO_4	5365 mF cm^{-2}, 203 F cm^{-3} at 33 mA cm^{-2} 175 F g^{-1} at 0.39 A g^{-1}	＞125 F g^{-1} at 70 mA cm^{-2}	~99% 10,000	/	/	[12]
Basswood	Delignification	~55 mg cm^{-2} 1.5 mm	6 M KOH	846 mF cm^{-2}, 65 F g^{-1} 2.6 F cm^{-3} at 1 mA cm^{-2}	160 mF cm^{-2}, 20 F g^{-1} at 20 mA cm^{-2}	81.48% 15,000 20 mA cm^{-2}	9.04 Wh kg^{-1}	2.39 W kg^{-1},	[7]

References

1. V. Augustyn, P. Simon and B. Dunn, Pseudocapacitive oxide materials for high-rate electrochemical energy storage, *Energy Environ. Sci.*, 2014, **7**, 1597.
2. G. Yuan, Y. Liang, H. Hu, H. Li, Y. Xiao, H. Dong, Y. Liu and M. Zheng, Extraordinary thickness-independent electrochemical energy storage enabled by cross-linked microporous carbon nanosheets, *ACS Appl. Mater. Interfaces*, 2019, **11**, 26946-26955.
3. F. Wang, J. Y. Cheong, Q. He, G. Duan, S. He, L. Zhang, Y. Zhao, I.-D. Kim and S. Jiang, Phosphorus-doped thick carbon electrode for high-energy density and long-life supercapacitors, *Chem. Eng. J.*, 2021, **414**, 128767.
4. F. Wang, J. Y. Cheong, J. Lee, J. Ahn, G. Duan, H. Chen, Q. Zhang, I. D. Kim and S. Jiang, Pyrolysis of enzymolysis-treated wood: Hierarchically assembled porous carbon electrode for advanced energy storage devices, *Adv. Funct. Mater.*, 2021, **31**, 2101077.
5. C. j. Chen, Y. Zhang, Y. Li, J. q. Dai, J. w. Song, Y. g. Yao, Y. h. Gong, I. Kierzewski, J. Xie and L. b. Hu, All-wood, low tortuosity, aqueous, biodegradable supercapacitors with ultra-high capacitance, *Energy Environ. Sci.*, 2017, **10**, 538-545.
6. Y. Katsuyama, N. Haba, H. Kobayashi, K. Iwase, A. Kudo, I. Honma and R. B. Kaner, Macro- and nano-porous 3D-hierarchical carbon lattices for extraordinarily high capacitance supercapacitors, *Adv. Funct. Mater.*, 2022, DOI: 10.1002/adfm.202201544, 2201544.
7. F. Wang, L. Zhang, Q. Zhang, J. Yang, G. Duan, W. Xu, F. Yang and S. Jiang, Electrode thickness design toward bulk energy storage devices with high areal/volumetric energy density, *Appl. Energy*, 2021, **289**, 116734.
8. X. Ma, X. Song, Z. Yu, S. Li, X. Wang, L. Zhao, L. Zhao, Z. Xiao, C. Qi, G. Ning and J. Gao, S-doping coupled with pore-structure modulation to conducting carbon black: Toward high mass loading electrical double-layer capacitor, *Carbon*, 2019, **149**, 646-654.
9. M. Vijayakumar, R. Santhosh, J. Adduru, T. N. Rao and M. Karthik, Activated carbon fibres as high performance supercapacitor electrodes with commercial level mass loading, *Carbon*, 2018, **140**, 465-476.
10. R. Zhang, J. Yan, L. Wang, W. Shen, J. Zhang, M. Zhong and S. Guo, Achieving ion accessibility within graphene films by carbon nanofiber intercalation for high mass loading electrodes in supercapacitors, *J. Power Sources*, 2021, **513**, 230559.
11. Z. Song, W. Li, Y. Bao, Z. Sun, L. Gao, M. H. Nawaz, D. Han and L. Niu, A new route to tailor high mass loading all-solid-state supercapacitor with ultra-high volumetric energy density, *Carbon*, 2018, **136**, 46-53.
12. M. Zhang, X. Yu, H. Ma, W. Du, L. Qu, C. Li and G. Shi, Robust graphene composite films for multifunctional electrochemical capacitors with an ultrawide range of areal mass loading toward high-rate frequency response and ultrahigh specific capacitance, *Energy Environ. Sci.*, 2018, **11**, 559-565.